# Service life prediction for 50-year-old buildings in marine environments

Agustín Sánchez-Deza[a], David M. Bastidas[b,✉], Angel La Iglesia[c],
Eleuterio M. Mora[a], José M. Bastidas[d]

[a] Naval Engineering School, Polytechnic University of Madrid (UPM), Av. Arco de la Victoria, 28040 Madrid, Spain
[b] National Center for Education and Research on Corrosion and Materials Performance, NCERCAMP-UA. Dept. of Chemical and Biomolecular Engineering. The University of Akron, 302 E Buchtel Ave, 44325-3906 Akron, OH, United States
[c] Institute of Geosciences (IGEO, CSIC), UCM, C/. José Antonio Novais 2, 28040 Madrid, Spain
[d] National Centre for Metallurgical Research (CENIM, CSIC), Av. Gregorio del Amo 8, 28040 Madrid, Spain
✉Corresponding Author: dbastidas@uakron.edu

**ABSTRACT:** Steel reinforcing bars are often coated with rusts formed during service in reinforced concrete (RC) structures. Rust layers growing on steel rebars induce expansive stresses and cause cracking on cover concrete. This study uses steel corrosion rate results measured on reinforced concrete buildings of more than 50 years of age located in marine environments and considers the pressure generated by the volume expansion of corrosion product layers to calculate the service life of the RC structures using a numerical simulation, estimating the time to corrosion cracking of the concrete cover. Akaganeite, goethite, lepidocrocite, hematite, magnetite and maghemite were identified by X-ray diffraction as crystalline phase constituents of the rust layers.

**KEYWORDS:** Chloride; Concrete corrosion cracking; Expansive stress; Marine environment; Rust layer

**RESUMEN:** *Predicción de la vida útil en servicio de edificios de 50 años expuestos a ambientes marinos.* Los refuerzos corrugados de acero embebidos en hormigón, presentan con frecuencia una capa de herrumbre formada durante la vida en servicio de las estructuras de hormigón armado (EHA). Las capas de óxido, productos de corrosión, que crecen en los refuerzos de acero inducen tensiones expansivas y causan el agrietamiento del recubrimiento de hormigón. El presente estudio utiliza los resultados de la velocidad de corrosión del acero corrugado, medidos en edificios de más de 50 años, construidos con hormigón armado, ubicados en ambientes marinos. El estudio considera la presión generada por la expansión de volumen de las capas de productos de corrosión para calcular la vida útil en servicio de las EHA utilizando una simulación numérica, estimando el tiempo hasta la fisuración por corrosión del recubrimiento de hormigón. Akaganeita, goethita, lepidocrocita, hematita, magnetita y maghemita fueron identificadas por difracción de rayos X, como constituyentes de las fases cristalinas de las capas de óxido.

**PALABRAS CLAVE:** Ambiente marino; Cloruros; Corrosión hormigón; Herrumbre; Tensión expansiva

**ORCID ID:** Agustín Sánchez-Deza (https://orcid.org/0000-0003-4078-9010); David M. Bastidas (https://orcid.org/0000-0002-8720-7500); Angel La Iglesia (https://orcid.org/0000-0002-2026-4279); Eleuterio M. Mora (https://orcid.org/0000-0002-9093-9542); José M. Bastidas (https://orcid.org/0000-0001-9616-0778)

# 1. INTRODUCTION

Degradation of RC structures is an issue of great importance and can severely shorten their service life. The highly alkaline environment (pH above 12.5) of a good quality concrete leads to the formation of an iron oxyhydroxide passive film (~10 nm) on the embedded steel, protecting it from corrosion and assuring a low steel corrosion rate of less than 1.16 μm/year (<0.10 μA·cm$^{-2}$) (González *et al.*, 1996; Fajardo *et al.*, 2011). However, this protective passive film can be disrupted when the pH of the concrete pore solution is lowered, e.g. by environmentally-induced carbonation, or when aggressive chloride ions from de-icing salts, direct contact with seawater or exposure to marine aerosols reach the reinforcements or are added directly during the mixing process as an ingredient, enabling diffusion to the steel surface (Chung *et al.*, 2008). Chloride ingress into concrete depends on the porosity (Jaegermann, 1990), chloride binding ability of the cementitious matrix (Rasheeduzzafar *et al.,* 1990), fissure characteristics (Mangat and Gurusamy, 1987), parameters such as relative humidity and temperature (Page *et al.*, 1981), concrete carbonation (Bertolini *et al.*, 2004), and saturation degree of the concrete porous network (Nielsen and Geiker, 2003).

Given that the specific volume of the iron oxyhydroxides formed during the corrosion process is larger than that of the original metallic iron, the rust layers growing on steel rebars in service may lead to various forms of corrosion-induced damage, such as cracking and spalling of the concrete cover, along with a loss of bonding between the concrete and the rebars, in particular if a thin concrete cover over the reinforcing steel was designed, thus leading to a reduction in the load-bearing capacity of the RC structure due to loss of bonding and loss of reinforcing steel section. The concrete cover spalling process caused by the difference in volume between iron oxyhydroxides and the original metallic iron has been reported in the literature (Suda *et al.*, 1993; Topçu *et al.*, 2010; Lu *et al.*, 2011; Zhao *et al.*, 2012; Cao *et al.*, 2013). However, the cracking mechanisms by which reinforced cover concrete is damaged in service are fully understood only in simplified laboratory simulated conditions and in clear and ideal environments.

Analytical efforts have been made to propose a model to predict either the residual flexural strength of RC beams subjected to reinforcement corrosion or the time to corrosion-induced cover cracking of the corroded RC structures. Some models discuss the time needed to generate cracking of the concrete as a function of the concrete characteristics, its physical properties and the accumulation of corrosion products (Liu and Weyers, 1998; Pantazopoulou and Papoulia, 2001), or assume good adherence behaviour at the steel/concrete interface to obtain an expansion threshold below which no crack propagation occurs (Leung, 2001). Other authors have modelled the critical corrosion penetration to initiate cracking and its relation with the reinforcement diameter (Andrade *et al.*, 1993; Torres-Acosta and Martínez-Madrid, 2003; Muñoz *et al.*, 2007; Torres-Acosta and Castro-Borges, 2013), or the reduction in the steel section due to corrosion considering the concrete cover/rebar diameter relation and the characteristics of the concrete (Vidal *et al.*, 2004; Bossio *et al.*, 2015; Fahy *et al.*, 2017).

The aim of this paper is to shed light on the service lifetime of RC structures with corrosion problems and to apply available whole-life service procedures by analysing the corrosion products generated on more than 50-year-old RC structures. A model was used to predict the time to cracking of the concrete cover based on the long-term steel corrosion rates of the RC structures determined by optical microscopy techniques.

# 2. EXPERIMENTAL

Corroded steel samples from four buildings located approximately 100 m from the shoreline on the Mediterranean coast of Spain and directly receiving chloride salt sprays were analysed. The buildings, at Alicante (samples labelled Alicante-I, Alicante-II and Alicante-III) and Barcelona, were constructed in the 1960's and had an average age of ~50 years. Samples of 50 cm in length were taken during the restoration of the buildings. Uniform corrosion and pitting corrosion was observed on the samples. The samples were stored in a desiccator to avoid exposure to the air during storage and transport before experimentation.

For the corrosion study, steel rebars of 5 mm in diameter from the four buildings were selected and cut using a diamond disc cooled with liquid paraffin, obtaining samples with dimensions of 25 × 25 × 30 mm. The surface of the samples was polished using alumina paste (Al$_2$O$_3$) of 20 μm grain size dispersed in paraffin, which was used for both cutting and polishing instead of water in order to avoid the dissolution of soluble chlorides.

The samples were analysed using a JEOL JSM-6400 scanning electron microscope (SEM), equipped with a LINK System energy-dispersive X-ray (EDX) microanalyser, operating in secondary electron (SE) and backscattered electron (BSE) imaging modes.

The corroded steel rebars were scraped to extract the corrosion products present on the samples and then characterised by X-ray diffraction (XRD) using a Bruker D8 Advance diffractometer equipped with Sol-X detector. The qualitative and quantitative crystalline composition was elucidated from XRD patterns by means the JCPDS database and EVA software from Bruker. The rust composition was determined using X-ray fluorescence (XRF)

spectroscopy on a Panalytical Axios spectrometer. Each result is the average of more than three determinations.

Optical microscopy techniques were used to determine the steel loss due to the corrosion process. The conversion of steel loss ($m$) into corrosion rate was determined using the Faraday's law: $m = (M/Fz) i_{corr} t$, where $m$ is the weight loss due to corrosion (g), $M$ is the atomic weight of the iron being dissolved (55.8 g·mol$^{-1}$), $F$ is the Faraday constant (96485 C·mol$^{-1}$), $z$ is the ionic charge of iron ($z = 2$) (Rémazeilles and Refait, 2007), $i_{corr}$ is the corrosion current density (A·cm$^{-2}$), and $t$ is the experimentation time (s). For steel, this gives a conversion factor of 11.6 µm/year = 1 µA·cm$^{-2}$ in the case of uniform corrosion. Possible disadvantages of using Faraday's equation are that the original weight of the tested rebar sections is unkown and the nominal section is different to the real section. The corrosion process is probably more complex than the simple generation of Fe$^{2+}$ ions during the 50-year exposure time, and a combination of several reactions with other ions during the service life of the buildings is more realistic.

## 3. RESULTS AND DISCUSSION

Figure 1 shows a SEM cross-section micrograph of a 5 mm diameter steel rebar embedded in the concrete belonging to building Alicante-I. Uniform corrosion can be observed along the steel/rust interface, despite the irregular shape of the rust/concrete interface. The rust layer developed has a thickness of 230–340 µm. Considering 50 years of exposure to the marine environment, a high corrosion rate can be estimated, in the range of 5–8 µm/year (0.43–0.69 µA·cm$^{-2}$) in the rust, which corresponds to 1.7−2.7 µm/year (0.15−0.23 µA·cm$^{-2}$) in the steel, considering a molar volume ratio coefficient ($\alpha$) of

expansion corrosion products to iron with a value of $\alpha$=2.94. These corrosion rates are about two to three times higher than for steel in the passive state, as indicated above <0.10 µA·cm$^{-2}$ (González *et al.* 1996). A multitude of pores (or voids) (see the arrows labelled: v) of a thickness of between 10 and 30 µm can be seen in the rust layer (see Fig. 1), along with the formation of many cracks in a radial direction.

Figure 2 shows a SEM micrograph of some of the cracks of Fig.1 which start in the rust layer and continue into the bulk concrete. Both Figs. 1 and 2 show the inclusion of concrete particles of 20−50 µm size in the porous rust layer, see the arrows labelled: c, in Figs. 1 and 2.

Figure 3 shows a SEM micrograph of the line profile analysis of Fe and Cl performed on each of the three layers (concrete, rust and steel) of Fig. 2. It can be observed that the rust layers contain a high chloride concentration, while this is very low in the concrete and the steel. Fig. 3 shows the inclusion of concrete particles in the porous rust layer, see the arrows labelled: c. Fig. 3 profile also shows the inclusion of one particle of concrete (~20 µm) in the rust layer as indicated above (see Fig. 1).

Figure 4 shows a SEM cross-section micrograph of a 5 mm diameter steel rebar embedded in the concrete belonging to building Alicante-II, depicting an irregular rust layer with a thickness of 220–300 µm, showing banded solid phases and alveolus textures, probably suggesting a seasonal discontinuous deterioration, see the regions of Fig. 4 labelled: banded. Considering 50 years of exposure to the marine environment, a high corrosion rate can be estimated, in the range of 4–6 µm/year (0.34–0.52 µA·cm$^{-2}$) in the rust or 1.4−2.0 µm/year (0.11−0.18 µA·cm$^{-2}$) in the steel. Similar corrosion rates were measured for the samples from the Alicante-III and Barcelona buildings, ~6 µm/year (0.52 µA·cm$^{-2}$) in the rust or 2.0 µm/year (0.18 µA·cm$^{-2}$) in the steel.
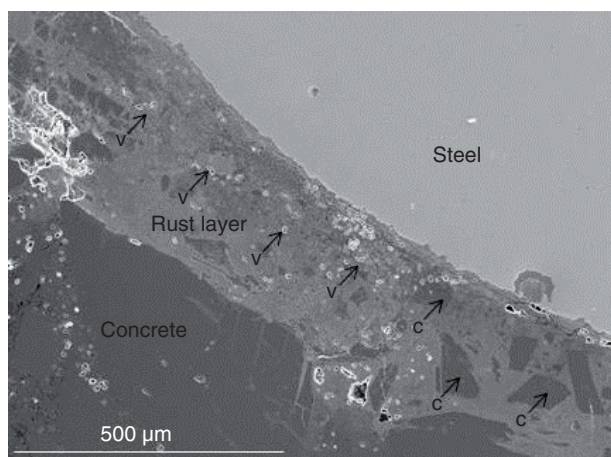


FIGURE 1. SEM micrograph of a reinforced concrete cross section of a corroded sample (Alicante-I) with a rust layer covering about 40% of the steel rebar, showing voids (v) and concrete particles (c).
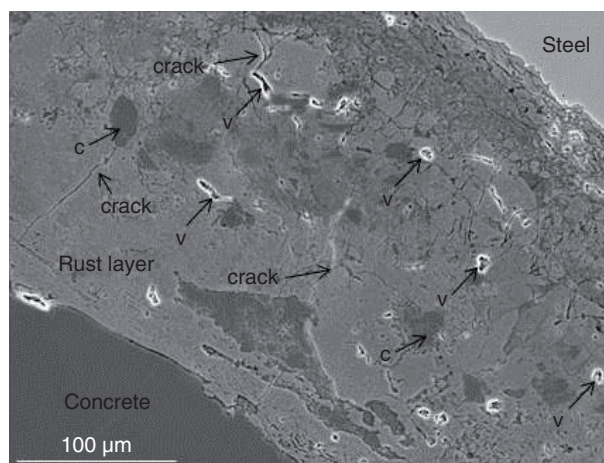


FIGURE 2. SEM micrograph of the cracks of the sample of Fig. 1, showing voids (v) and concrete particles (c).
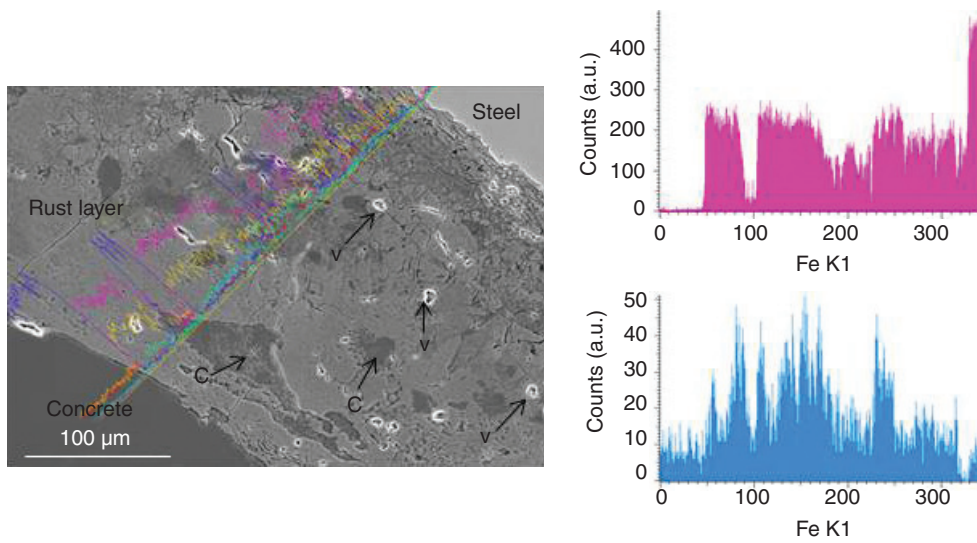
FIGURE 3.    SEM micrograph and line profile analysis of Fig. 2 of the steel/concrete interface.
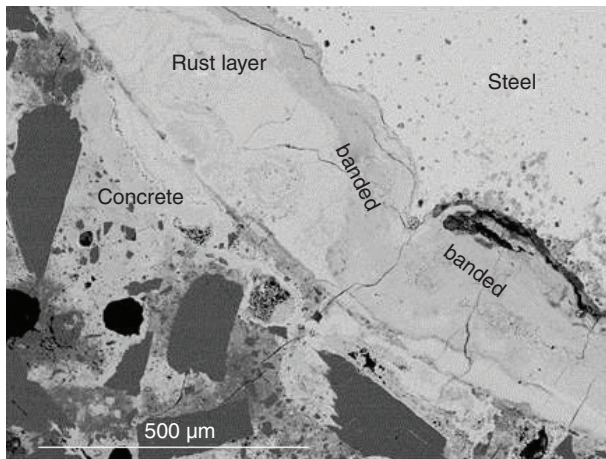


FIGURE 4.    SEM micrograph of a cross section of a corroded sample (Alicante II) with a rust layer covering about 40–50% of the rebar.
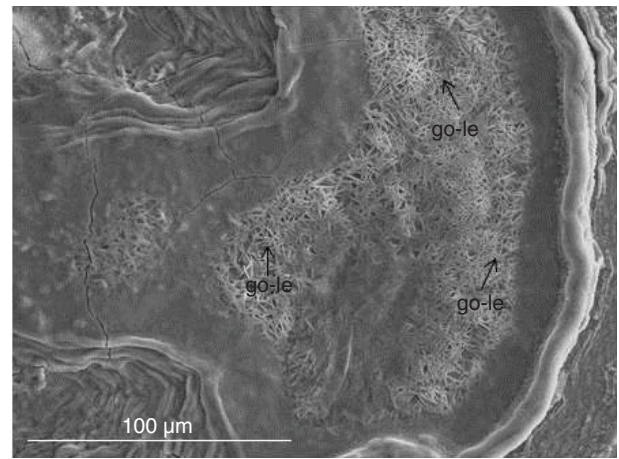


FIGURE 5.    SEM micrograph of a cross section of the corroded sample of Fig. 4.

Fig. 4 also shows the formation of many cracks in radial direction originated in the rust layers and propagated through the concrete cover. The line profile analyses were similar to the sample of Fig. 3 (Alicante-I), with a high chloride concentration in the rust layers and a very low concentration in the concrete and steel. Fig. 5 shows a SEM micrograph of the fibrous particles ("grouped like a honeycomb") growing inside the pores, which may correspond to goethite-lepidocrocite phases, see the arrows labelled: go-le. Finally, Fig. 6 displays representative XRD patterns for the four samples studied.

Table 1 indicates the crystalline XRD composition (%) of the studied samples. The six phases identified in the rust layers are: akaganeite ($Fe_8O_8(OH)_8Cl_{1.36}$), goethite ($\alpha$-FeOOH), lepidocrocite ($\gamma$-FeOOH), hematite ($\alpha$-$Fe_2O_3$), magnetite ($Fe_3O_4$) and maghemite ($\gamma$-$Fe_2O_3$), which are described in the literature as the main components of rust layers (Suda *et al.*, 1993; Torres-Acosta and Martínez-Madrid, 2003).

Table 2 displays the chemical composition (%) obtained by XRF analysis of the samples from Alicante-I, Alicante-II, Alicante-III and Barcelona.

Figure 7 shows the variation in akaganeite (%) (determined by XRD) versus the chloride content (%) (determined by XRF) for the four samples, which presents a linear variation, indicating the goodness of XRD technique to quantify the akaganeite phase. The highest akaganeite content (52%) (see Table 1) was yielded on samples with the highest chloride content (2.05%) (see Table 2). This result agrees well with the atmospheric corrosion of steel, as a Cl⁻ threshold of 60 mg·m⁻²·day⁻¹ and simultaneously a relative humidity of around 80% to be necessary for the formation of akaganeite (Morcillo *et al.*, 2015).
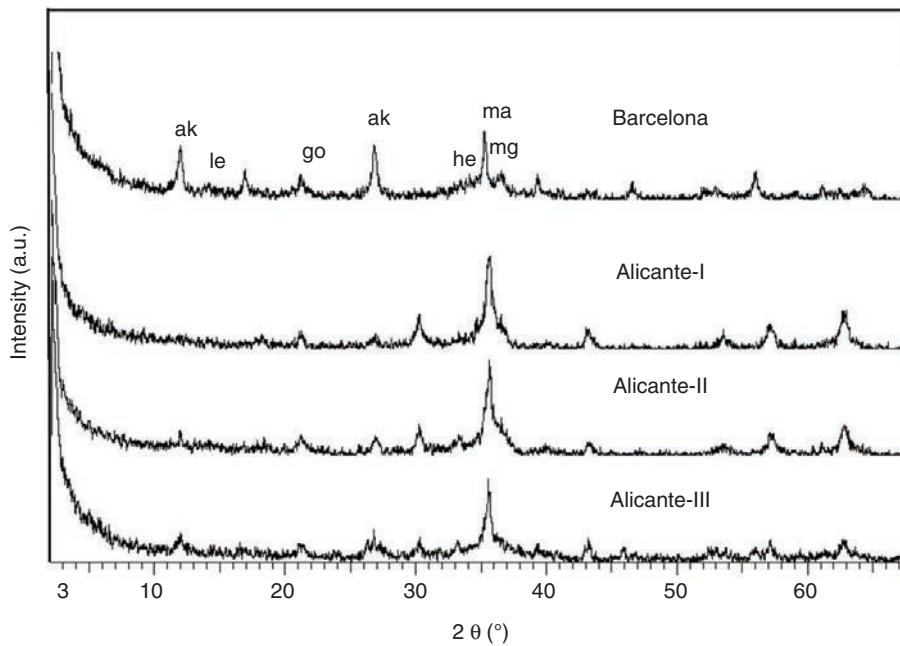
FIGURE 6.    XRD patterns for rust layers formed on steel rebars from Barcelona, Alicante-I, Alicante-II and Alicante-III. ak: Akagaenite, go: Goethite, le: Lepidocrocite, he: Hematite, ma: Magnetite, mg: Maghemite.

TABLE 1. Composition of the crystalline phases (% wt.) determined by X-ray diffraction (XRD)

| Building | Akaganeite $Fe_8O_8(OH)_8Cl_{1.36}$ | Goethite $\alpha$-FeOOH | Lepidocrocite $\gamma$-FeOOH | Hematite $\alpha$-$Fe_2O_3$ | Magnetite $Fe_3O_4$ | Maghemite $\gamma$-$Fe_2O_3$ |
|---|---|---|---|---|---|---|
| Barcelona | 52 | 11 | 9 | 7 | 19 | 2 |
| Alicante-I | 27 | 13 | 5 | 7 | 35 | 13 |
| Alicante-II | 20 | 7 | 4 | 0 | 44 | 25 |
| Alicante-III | 40 | 10 | 5 | 0 | 29 | 16 |

TABLE 2. Chemical composition (% wt.) determined by X-ray fluorescence (XRF)

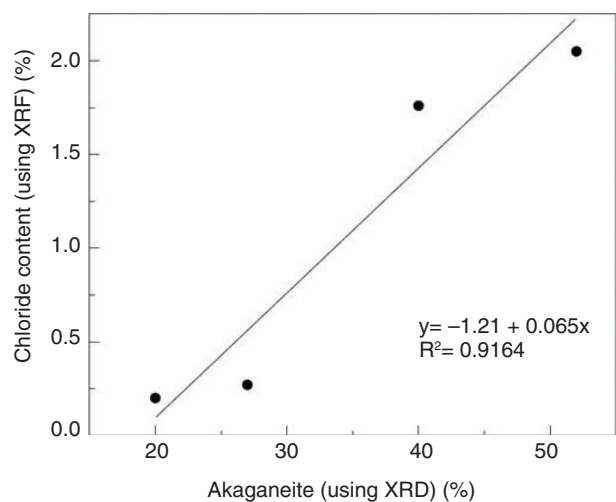| Element | Alicante-I | Alicante-II | Alicante-III | Barcelona |
|---|---|---|---|---|
| Fe | 67.67 | 60.87 | 68.75 | 66.58 |
| O | 30.16 | 30.49 | 30.08 | 29.60 |
| Mn | 0.82 | 0.28 | 0.53 | 0.41 |
| Al | 0.09 | 0.11 | 0.10 | 0.09 |
| Si | 0.34 | 0.25 | 0.12 | 0.25 |
| Cl | 0.27 | 1.75 | 0.20 | 2.05 |
| Ca | 0.37 | 4.02 | 0.14 | 0.16 |
| P | 0.02 | 0.06 | 0.04 | 0.07 |
| S | 0.04 | 1.19 | 0.03 | 0.11 |
| Zn | 0 | 0.36 | 0 | 0.33 |
| Mg | 0.20 | 0.43 | 0 | 0 |
| Cu | 0 | 0 | 0 | 0.17 |
| Na | 0 | 0 | 0 | 0 |
| K | 0 | 0.07 | 0 | 0.09 |



$y= -1.21 + 0.065x$
$R^2= 0.9164$

FIGURE 7.    Variation in akaganeite (%) (determined using XRD) as a function of chloride content in the rust layers (%) (determined using XRF).

Table 3 presents the molar volume ratio coefficient ($\alpha$) of expansive rust layer to iron consumed in the corrosion, obtained from JCPDS database and (Robie *et al*., 1979):

$$\alpha = V_{m(oxide)}/V_{m(Fe)} \qquad (1)$$

The $\alpha$ coefficient indicates the increase in volume during the oxidation process, which leads to a pressure increase if the oxidation process takes place in a confined space (Sanz *et al*., 2015). The $\alpha$ values yielded were in the following order from high to low: akaganeite > lepidocrocite > goethite > maghemite > hematite > magnetite. The high $\alpha$ coefficient of akaganeite (3.59) may accelerate the cracking process more than the other five mineral phases, lepidocrocite (3.16), goethite (2.94), maghemite (2.30), hematite (2.13) and magnetite (2.09).

On the mechanism by which the reinforced concrete cover is damaged, it is known that concrete in outdoor exposure conditions is subjected to oscillations of environmental parameters that vary the corrosion rate and need to be known in order to establish the state of conservation of the structure. The rust layers on steel exposed to outdoor atmospheric environments are porous and poorly adherent. Pore sizes with typical pore volumes constituting 5–10% of the rust volume have been found, such a structure allows the ingress of water (Graedel and Frankenthal, 1990). In the formation of these rust layers, iron released from the steel is initially oxidised to ferrous ion.

In order to predict the time to cracking of cover concrete on corroded RC structures in marine environments using a numerical model, it was assumed that the spatially corrosion products formed around the steel rebar surface generate a thick-walled cylinder approach. A porous network is also assumed to exist around the steel/concrete interface, an assumption corroborated by Figs. 1 and 2.

When the corrosion products exceeds that required to fill up the porous zone it causes pressure on the surrounding cover, inducing the following three steps: (i) it is assumed that the concrete cover presents elastic behaviour until the stress at the steel/concrete interface reaches the concrete's tensile strength ($f_t$), during this step, the pressure is determined and governed by the balance of volume variations between the steel rebar ($\Delta V_s$), concrete cover ($\Delta V_c$) and the rust formed under pressure ($V_{rc}$), Eq. (2):

$$\Delta V_s + \Delta V_c = V_{rc} \qquad (2)$$

(ii) In the second step, the crack propagates through the concrete cover while the tangential stress ($\sigma_t$) exceeds the $f_t$. The uncracked part of the cover is treated as a thick-walled cylinder and the front of the crack ($R_c$) is ruled by the cubic Eq. (3) (Balafas and Burgoyne, 2011):

$$f_t R_c^3 + R_{ci} p R_c^2 - (R_{ci} + c)^2 f_t R_c + (R_{ci} + c)^2 R_{ci} p = 0 \quad (3)$$

where $f_t$ is the concrete tensile strength, $c$ is the concrete cover depth thickness or clear cover to the reinforcement, $R_c$ (the crack front length of concrete) and whenever this variable exceeds the ~13 mm threshold leads to cracking of the concrete, $R_{ci}$ is the radius at the initiation of the crack (2.5 mm), and $p$ is the pressure.

(iii) Finally, in the third step the cover fails. The crack propagates uniformly through the concrete cover when the energy release rate ($G_R$) is lower than the fracture energy of the concrete ($G_F$), after which the cover fails. The $G_R$ parameter has been calculated taking into account the strain energy of the elastic ring cover concrete ($SE_e$), strain energy of cracked ring cover concrete ($SE_c$) and strain energy of steel ($SE_s$) and assuming a negligible strain energy of the rust, Eq. (4) (Achintha and Burgoyne, 2008):

$$G_R = \frac{SE_e + SE_c + SE_s}{R_b + c - R_c} \qquad (4)$$

where $R_b$ is the reinforcement steel radius, see Table 4.

The numerical simulations of concrete cracking were performed on MATLAB Matrix Laboratory

TABLE 3. Crystalline phases found in the present study, molar volume ($V_m$), using the JCPDS database and Robie *et al*. (1979) as source, and molar volume expansion ratio coefficient ($\alpha$), $\alpha = V_{m(oxide)}/V_{m(Fe)}$

| Crystalline Phase | Molar Volume, $V_m$, (cm$^3$·mol$^{-1}$) | Molar Volume Expansion Ratio Coefficient, $\alpha = V_{m(oxide)}/V_{m(Fe)}$ |
|---|---|---|
| Iron ($\alpha$-Fe) | 7.09[a] | – |
| Akaganeite (Fe$_8$O$_8$(OH)$_8$Cl$_{1.36}$) | 203.62[a] | 3.59 |
| Goethite ($\alpha$-FeOOH) | 20.82[b] | 2.94 |
| Lepidocrocite ($\gamma$-FeOOH) | 22.42[a] | 3.16 |
| Hematite ($\alpha$-Fe$_2$O$_3$) | 30.27[b] | 2.13 |
| Magnetite (Fe$_3$O$_4$) | 44.52[b] | 2.09 |
| Maghemite ($\gamma$-Fe$_2$O$_3$) | 32.63[a] | 2.30 |

[a]JCPDS database.
[b]Robie *et al*. (1979).

software and following the modelling detailed by (Balafas and Burgoyne, 2011). The corrosion current densities ($i_{corr}$) used in the simulation were: 0.15, 0.20, 0.25, 0.35, 0.50, 0.75, 1.00 and 1.50 μA·cm$^{-2}$.

TABLE 4. Mechanical properties of the steel, concrete and rust, and parameters used in the numerical simulation

| Steel Properties | |
|---|---|
| Poisson's Coefficient ($v_{st}$) | 0.28 |
| Elastic Modulus ($E_{st}$) (GPa) | 210 |
| Density ($\rho_{st}$) (g·cm$^{-3}$) | 7.85 |
| Reinforcement Steel Radius ($R_b$) (mm) | 2.5 |
| **Concrete Properties** | |
| Poisson's Coefficient ($v_{co}$) | 0.20 |
| Elastic Modulus ($E_{co}$) (GPa) | 20 |
| Fracture Energy ($G_F$) (N·mm$^{-1}$) | 0.12 |
| Tensile Strength ($f_t$) (MPa) | 2.6 |
| Concrete Cover Depth Thickness ($c$) (mm) | 15 |
| Concrete Ring Porous Thickness ($d_0$) (mm) | 10 |
| **Rust Properties** | |
| Bulk Modulus ($K_{ru}$) (kN·mm$^{-2}$) | 0.60 |
| Elastic Modulus ($E_r$) (MPa) | 20 |
| Mass Ratio of Iron to Rust ($r_m$) | 0.643 |
| Volume Expansion Ratio Coefficient ($\alpha$) | 2.94 |
| Rust Layers Diffusion Coefficient ($n_l$) | 2 |
| Reduction of Corrosion Rate Due to Rust Thickness Coefficient ($k_{coef}$) | 0.086 |

These $i_{corr}$ values were used in order to cover a wide steel corrosion rate range, more than that experimentally measured: 0.34–0.69 μA·cm$^{-2}$ in the rust or 0.11–0.23 μA·cm$^{-2}$ in the steel, in the buildings located in marine environments indicated above. The input parameters of the steel, concrete and rust properties used in the numerical simulation are included in Table 4. A value of molar volume expansion ratio coefficient α=2.94 was selected as a representative intermediate value for goethite. The output results of the numerical simulations have been used to draw Figs. 8 to 11.

Figure 8 shows the pressure ($p$) generated by the rust growing at the rust/concrete interface, as a function of time due to corrosion for current density ($i_{corr}$) values from 0.15 to 1.50 μA·cm$^{-2}$. The curves show the failure pressure, between 6.5 and 7.5 MPa, which is reached soon for the highest $i_{corr}$ value (1.50 μA·cm$^{-2}$). The $p$ parameter increases and reaches a peak value when the crack propagates on the concrete cover. It can be observed that for a given value of $p$ the time required for cover cracking increases as the $i_{corr}$ decreases. This is a value of practical importance because seasonal changes lead to different steel corrosion rates and may accelerate the failure of the concrete cover.

Figure 9 shows the variation in the crack front radius ($R_c$) versus time (months) for different $i_{corr}$ values. As for pressure ($p$) (Fig. 8) the $R_c$ increases and reaches a peak value at around 13 mm, where the crack propagates on the cover concrete leading to service failure of the RC structure.
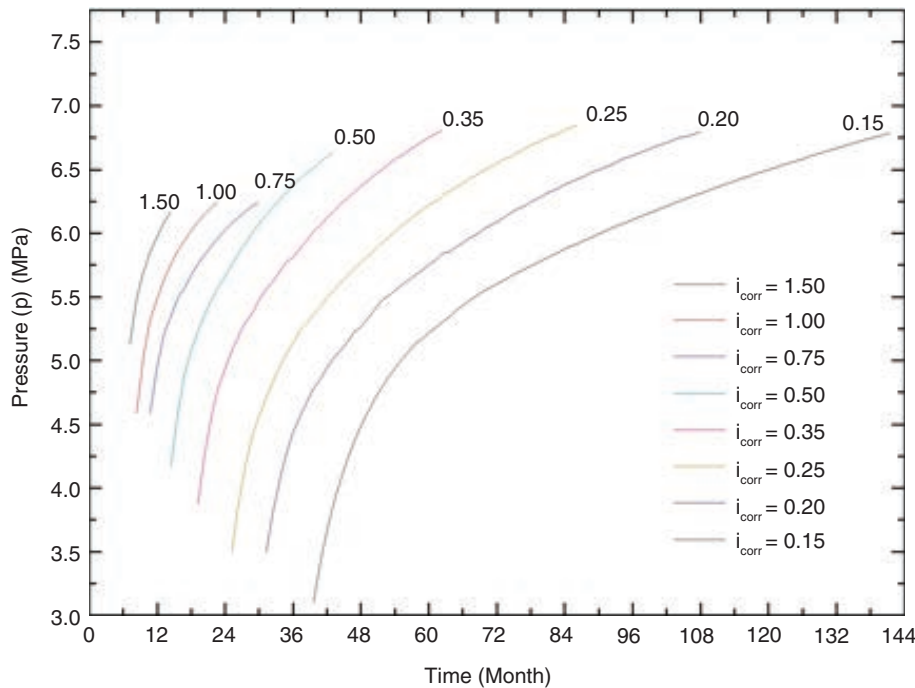


FIGURE 8. Pressure build-up versus time at rust/concrete interface for different corrosion current density ($i_{corr}$) values: 0.15, 0.20, 0.25, 0.35, 0.50, 0.75, 1.00 and 1.50 μA·cm$^{-2}$.
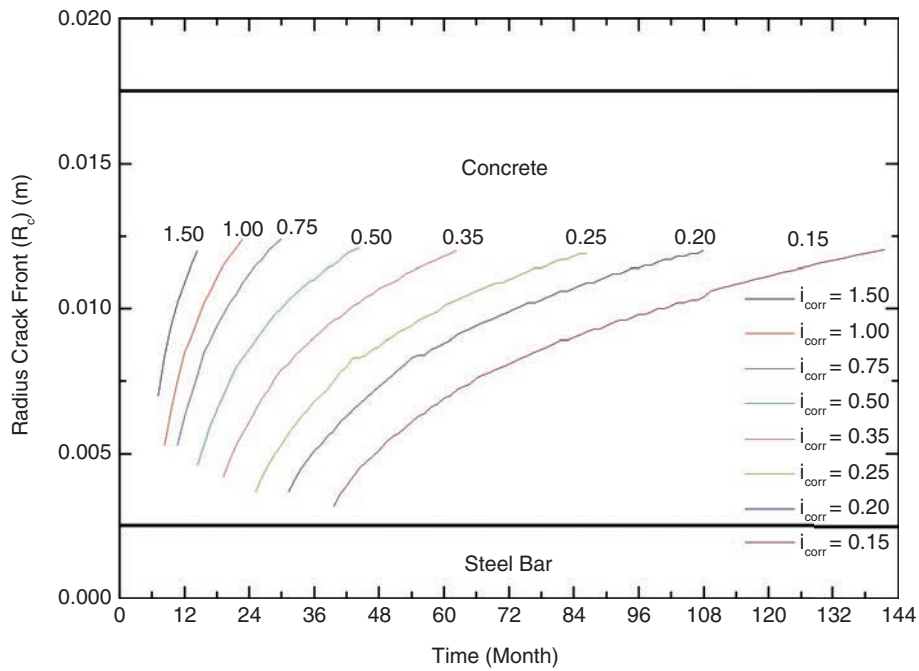
FIGURE 9.   Crack front radius ($R_c$) versus time for different corrosion current density ($i_{corr}$) values: 0.15, 0.20, 0.25, 0.35, 0.50, 0.75, 1.00 and 1.50 µA·cm$^{-2}$. Horizontal lines indicate a frontal view of steel and concrete cover.
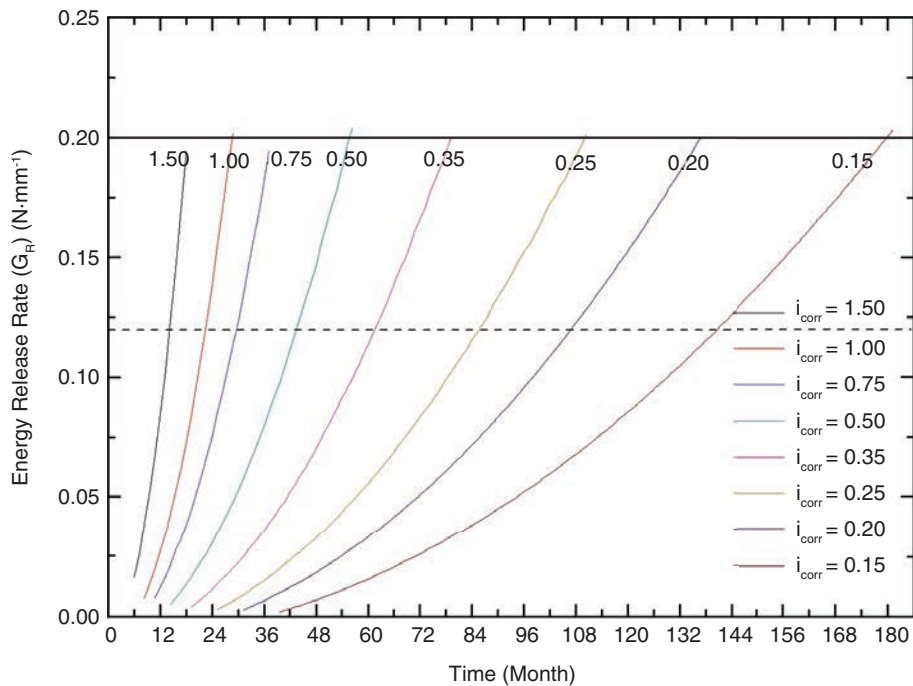


FIGURE 10.   Energy release rate ($G_R$) versus time for different corrosion current density ($i_{corr}$) values: 0.15, 0.20, 0.25, 0.35, 0.50, 0.75, 1.00 and 1.50 µA·cm$^{-2}$. Dotted line for normal strength concrete, and continuous line for high strength concrete.

Figure 10 shows the variation in the energy release rate ($G_R$) versus time (months) for different corrosion current density ($i_{corr}$) values. If $G_R$ is equal to or greater than the fracture energy of the concrete ($G_F$), and provided it exceeds the 0.12 N·mm$^{-1}$ (normal strength, see dotted line) or the 0.2 N·mm$^{-1}$ (high strength, see continuous line) threshold, the concrete cover fails.
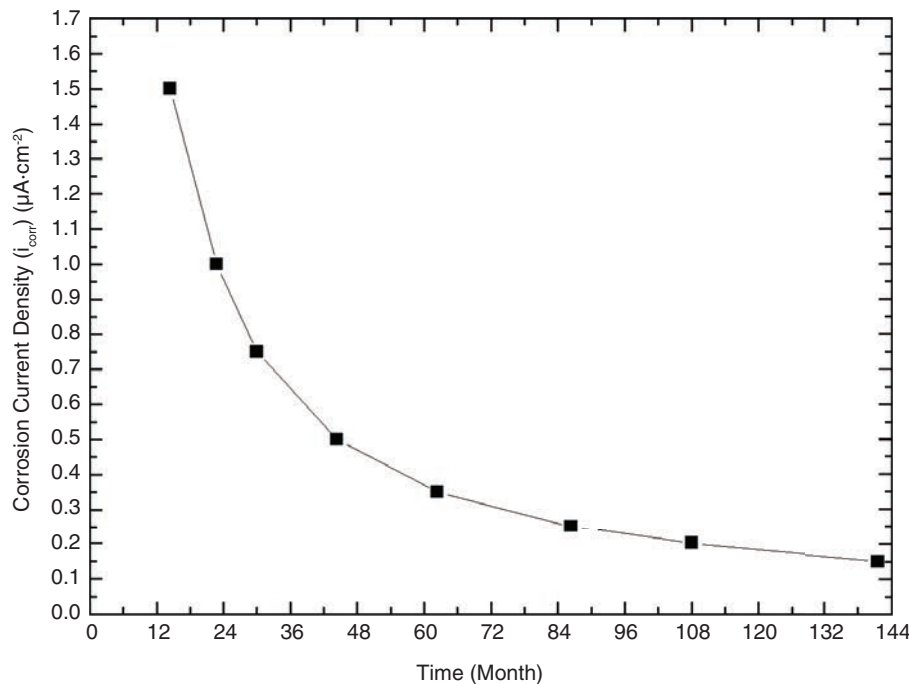
FIGURE 11.    Variation in corrosion current density ($i_{corr}$) versus time to cracking. The $i_{corr}$ values used were: 0.15, 0.20, 0.25, 0.35, 0.50, 0.75, 1.00 and 1.50 µA·cm$^{-2}$.

Figure 11 shows the variation in the corrosion current density ($i_{corr}$) versus time. The ability to predict the time to cover cracking is important marks the end of the structure's fully effective service life (Balafas and Burgoyne, 2011).

As can be observed in Fig. 11, the time to cracking decreases exponentially when the steel corrosion rate ($i_{corr}$) rises. This result agrees well with the energy release rate ($G_R$) of Fig. 10, and with the crack front radius ($R_c$) of Fig. 9. Thus, the simple numerical model used suggests that the risk of concrete cover cracking may be due to steel corrosion rates higher than 0.10 µA·cm$^{-2}$ (1.16 µm/year), which is easy to reach in a marine environment. Additionally, the probability of akaganeite formation (which is also particularly high in a marine environment), with a high volume expansion ratio coefficient ($\alpha$) value of 3.59, makes it a harmful crystalline phase. In the current study a representative intermediate value of 2.94 was used for the $\alpha$ coefficient, see Table 4.

## 4. CONCLUSIONS

-   The volume expansion ratio coefficient ($\alpha$) of the identified crystalline phases, and consequently their capacity to generate pressure in confined spaces, can be ordered from high to low as follows: akaganeite > lepidocrocite > goethite > maghemite > hematite > magnetite.

-   The Balafas-Burgoyne model can be used to assess concrete cover cracking as a consequence of pressure generated by the crystalline phases.
-   The pressure ($p$) and the crack front radius ($R_c$) increase with time and reach a peak value when the crack propagates on the concrete cover.
-   These peak values and the 0.12 N·mm$^{-1}$ threshold for the energy release rate ($G_R$) are reached as quickly as the corrosion rate increases from 0.15 to 1.50 µA·cm$^{-2}$.
-   For a concrete cover depth thickness of 15 mm in a marine environment, akaganeite is the most harmful oxide for the service life of the RC structure.

## REFERENCES

Achintha, P.M.M., Burgoyne, C.J. (2008). Fracture mechanism of plate debonding. *J. Compos. Constr.* 12 (4), 396–404. https://doi.org/10.1061/(ASCE)1090-0268(2008)12:4(396).
Andrade, C., Alonso, C., Molina, F.J. (1993). Cover cracking as a function of bar corrosion: Part I-Experimental test. *Mater. Struct.* 26 (8), 453–464. https://doi.org/10.1007/BF02472805.

Balafas, I., Burgoyne, C.J. (2011). Modeling the structural effects of rust in concrete cover. *J. Eng. Mech.-ASCE* 137 (3), 175–185. https://doi.org/10.1061/(ASCE)EM.1943-7889.0000215.

Bertolini, L., Elsener, B., Pedeferri, P., Polder, R. (2004). *Corrosion of Steel in Concrete: Prevention, Diagnosis, Repair*. Wiley-VCH, Weinheim, Germany. https://doi.org/10.1002/3527603379.

Bossio, A., Monetta, T., Bellucci, F., Lignola, G.P., Prota, A. (2015). Modeling of concrete cracking due to corrosion process of reinforcement bars. *Cement Concrete Res*. 71, 78–92. https://doi.org/10.1016/j.cemconres.2015.01.010.

Cao, C., Cheung, M.M.S., Chan, B.Y.B. (2013). Modelling of interaction between corrosion-induced concrete cover crack and steel corrosion rate. *Corros. Sci*. 69, 97–109. https://doi.org/10.1016/j.corsci.2012.11.028.

Chung, L., Najm, H., Balaguru, P. (2008). Flexural behavior of concrete slabs with corroded bars. *Cement Concrete Comp*. 30 (3), 184–193. https://doi.org/10.1016/j.cemconcomp.2007.08.005.

Fahy, C., Wheeler, S.J., Gallipoli, D., Grassi, P. (2017). Corrosion induced cracking modelled by a coupled transport-structural approach. *Cement Concrete Res*. 94, 24–35. https://doi.org/10.1016/j.cemconres.2017.01.007.

Fajardo, S., Bastidas, D.M., Criado, M., Romero, M., Bastidas, J.M. (2011). Corrosion behaviour of a new low-nickel stainless steel in saturated calcium hydroxide solution. *Constr. Build. Mater*. 25 (1), 4190–4196. https://doi.org/10.1016/j.conbuildmat.2011.04.056.

González, J.A., Ramírez, E., Bautista, A., Feliu, S. (1996). The behaviour of pre-rusted steel in concrete. *Cement Concrete Res*. 26 (3), 501–511. https://doi.org/10.1016/S0008-8846(96)85037-X.

Graedel, T.E., Frankenthal, R.P. (1990). Corrosion mechanisms for iron and low alloy steels exposed to the atmosphere. *J. Electrochem. Soc*. 137 (8), 2385–2394. https://doi.org/10.1149/1.2086948.

Jaegermann, C. (1990). Effect of water-cement ratio and curing on chloride penetration into concrete exposed to Mediterranean sea climate. *ACI Mater. J*. 87 (4), 333–339. https://doi.org/10.14359/2039.

Leung, C.K.Y. (2001). Modeling of concrete cracking induced by steel expansion. *J. Mater. Civil Eng*. 13 (3), 169–175. https://doi.org/10.1061/(ASCE)0899-1561(2001)13:3(169).

Liu, Y., Weyers, R.E. (1998). Modeling the time-to-corrosion cracking in chloride contaminated reinforced concrete structures. *ACI Mater. J*. 95 (6), 675–680. https://doi.org/10.14359/410.

Lu, C., Jin, W., Liu, R. (2011). Reinforcement corrosion-induced cover cracking and its time prediction for reinforced concrete structures. *Corros. Sci*. 53 (4), 1337–1347. https://doi.org/10.1016/j.corsci.2010.12.026.

Mangat, P.S., Gurusamy, K. (1987). Chloride diffusion in steel fibre reinforced marine concrete. *Cement Concrete Res*. 17 (3), 385–396. https://doi.org/10.1016/0008-8846(87)90002-0.

Morcillo, M., González-Calbet, J.M., Jiménez, J.A., Díaz, I., Alcántara, J., Chico, B., Mazario-Fernández, A., Gómez-Herrero, A., Llorente, I., de la Fuente, D. (2015). Environmental conditions for akaganeite formation in marine atmosphere mild steel corrosion products and its characterization. *Corrosion* 71 (7), 872–886. https://doi.org/10.5006/1672.

Muñoz, A., Andrade, C., Torres, A., Rodríguez, J. (2007). Relation between crack width and diameter of rebar loss due to corrosion of reinforced concrete members. *ECS Transactions* 3 (13), 29–36. https://doi.org/10.1149/1.2721428.

Nielsen, E.P., Geiker, M.R. (2003). Chloride diffusion in partially saturated cementitious material. *Cement Concrete Res*. 33 (1), 133–138. https://doi.org/10.1016/S0008-8846(02)00939-0.

Page, C.L., Short, N.R., El Tarras, A. (1981). Diffusion of chloride ions in hardened cement pastes. *Cement Concrete Res*. 11 (3), 395–406. https://doi.org/10.1016/0008-8846(81)90111-3.

Pantazopoulou, S.J., Papoulia, K.D. (2001). Modeling cover-cracking due to reinforcement corrosion in RC structures. *J. Eng. Mech.-ASCE* 127 (4), 342–351. https://doi.org/10.1061/(ASCE)0733-9399(2001)127:4(342).

Rasheeduzzafar, Al-Saadoun, S.S., Al-Gahtani, A.S., Dakhil, F.H. (1990). Effect of tricalcium aluminate content of cement on corrosion of reinforcing steel in concrete. *Cement Concrete Res*. 20 (5), 723–738. https://doi.org/10.1016/0008-8846(90)90006-J.

Rémazeilles, C., Refait, Ph. (2007). On the formation of β–FeOOH (akaganéite) in chloride-containing environments. *Corros. Sci*. 49 (2), 844–857. https://doi.org/10.1016/j.corsci.2006.06.003.

Robie, R.A., Hemingway, B.S., Fisher, J.R. (1979). *Thermodynamic properties of minerals and related substances at 298.15 K and 1 Bar ($10^5$ Pascal) pressure and at higher temperatures*. Report, Bulletin 1452, Publisher: U.S. Geological Survey, USA.

Sanz, B., Planas, J., Sancho, J.M. (2015). A closer look to the mechanical behavior of the oxide layer in concrete reinforcement corrosion. *Int. J. Solids Struct*. 62, 256–268. https://doi.org/10.1016/j.ijsolstr.2015.02.040.

Suda, K., Misra, S., Motohashi, K. (1993). Corrosion products of reinforcing bars embedded in concrete. *Corros. Sci*. 35 (5–8), 1543–1549. https://doi.org/10.1016/0010-938X(93)90382-Q.

Topçu, I.B., Boğa, A.R., Demir, A. (2010). The effect of elevated temperatures on corroded and uncorroded reinforcement embedded in mortar. *Constr. Build. Mater*. 24 (11), 2101–2107. https://doi.org/10.1016/j.conbuildmat.2010.04.050.

Torres-Acosta, A.A., Castro-Borges, P. (2013). Corrosion-induced cracking of concrete elements exposed to a natural marine environment for five years. *Corrosion* 69 (11), 1122–1131. https://doi.org/10.5006/0844.

Torres-Acosta, A.A., Martínez-Madrid, M. (2003). Residual life of corroding reinforced concrete structures in marine environment. *J. Mater. Civil Eng*. 15 (4), 344–353. https://doi.org/10.1061/(ASCE)0899-1561(2003)15:4(344).

Vidal, T., Castel, A., François, R. (2004). Analyzing crack width to predict corrosion in reinforced concrete. *Cement. Concrete Res*. 34 (1), 165–174. https://doi.org/10.1016/S0008-8846(03)00246-1.

Zhao, Y., Yu, J., Wu, Y., Jin, W. (2012). Critical thickness of rust layer at inner and out surface cracking of concrete cover in reinforced concrete structures. *Corros. Sci*. 59, 316–323. https://doi.org/10.1016/j.corsci.2012.03.018.